
CALIBRATED BAYESIAN DEEP LEARNING FOR EXPLAINABLE DECISION SUPPORT SYSTEMS BASED ON MEDICAL IMAGING

Hua Xu

Escuela Técnica Superior de Ingenieros de Telecomunicación
Universidad Politécnica de Madrid
28040, Madrid, Spain
hua.xu@alumnos.upm.es

Julián D. Arias-Londoño

Escuela Técnica Superior de Ingenieros de Telecomunicación
Universidad Politécnica de Madrid
28040, Madrid, Spain
julian.arias@upm.es

Juan I. Godino-Llorente

Escuela Técnica Superior de Ingenieros de Telecomunicación
Universidad Politécnica de Madrid
28040, Madrid, Spain
ignacio.godino@upm.es

February 13, 2026

ABSTRACT

In critical decision support systems based on medical imaging, the reliability of AI-assisted decision-making is as relevant as predictive accuracy. Although deep learning models have demonstrated significant accuracy, they frequently suffer from miscalibration, manifested as overconfidence in erroneous predictions. To facilitate clinical acceptance, it is imperative that models quantify uncertainty in a manner that correlates with prediction correctness, allowing clinicians to identify unreliable outputs for further review. In order to address this necessity, the present paper proposes a generalizable probabilistic optimization framework grounded in Bayesian deep learning. Specifically, a novel Confidence-Uncertainty Boundary Loss (CUB-Loss) is introduced that imposes penalties on high-certainty errors and low-certainty correct predictions, explicitly enforcing alignment between prediction correctness and uncertainty estimates. Complementing this training-time optimization, a Dual Temperature Scaling (DTS) strategy is devised for post-hoc calibration, further refining the posterior distribution to improve intuitive explainability. The proposed framework is validated on three distinct medical imaging tasks: automatic screening of pneumonia, diabetic retinopathy detection, and identification of skin lesions. Empirical results demonstrate that the proposed approach achieves consistent calibration improvements across diverse modalities, maintains robust performance in data-scarce scenarios, and remains effective on severely imbalanced datasets, underscoring its potential for real clinical deployment.

Keywords Bayesian Deep Learning · Decision Support Systems · Uncertainty Quantification · Model Calibration · Explainable AI · Medical Image Analysis

1 Introduction

Deep learning has achieved remarkable advances in medical image analysis, demonstrating classification performance comparable to that of human experts across many application domains.

Predominantly, these approaches rely on deterministic deep neural networks, which operate on the maximum likelihood estimation principle by optimizing weights to minimize the negative log-likelihood loss. However, while effective in achieving high accuracy, this paradigm is prone to overfitting, often resulting in overconfidence [1]. This overconfidence obscures the distinction between reliable and unreliable predictions, leaving clinicians without a principled basis for deciding when to trust model outputs. Consequently, in critical healthcare applications, models must not only achieve high predictive accuracy but also quantify their predictive uncertainty, providing clinicians with an explicit indicator of output reliability to support informed decision-making [2, 3].

In this context, Bayesian Neural Networks (BNNs) offer a framework for uncertainty quantification by modeling weight distributions rather than point estimates [4, 5]. The implementation of BNNs necessitates a critical selection between approximation methods, most notably Monte Carlo (MC) Dropout [6] and Variational Inference (VI) [7, 8]. While MC Dropout offers computational convenience, it relies on a fixed Bernoulli distribution with a pre-defined dropout rate, inherently limiting the model's capacity to adaptively learn parameter-specific uncertainty [9]. In contrast, VI explicitly approximates the posterior distribution of weights by optimizing the Evidence Lower Bound (ELBO), allowing the model to derive the variance of each weight parameter directly from the data [7]. This approach facilitates a more expressive and fine-grained quantification of uncertainty, providing the rigorous probabilistic foundation required for high-stakes medical decision-making [3].

However, BNNs exhibits practical limitations in real-world medical imaging applications [10]. In particular, their predictive performance and uncertainty estimates often degrade under small-sample and severely imbalanced data regimes, which are prevalent in clinical datasets [11]. Moreover, although BNNs offers a principled framework for uncertainty quantification, the resulting uncertainty estimates are not inherently guaranteed to be decision-consistent -i.e., systematically low for correct predictions and high for incorrect ones-unless explicitly enforced through additional modeling or optimization constraints [12].

These limitations highlight the need for a unified optimization framework that explicitly enforces alignment between predictive correctness and uncertainty, while maintaining robustness across varying data scales, class distributions, and clinical tasks. Such a framework is essential to ensure both the reliability and general applicability of uncertainty-aware models in diverse medical imaging scenarios.

To address these challenges, this work proposes a generalizable probabilistic optimization framework grounded in BNNs. Rather than relying on task-specific architectural modifications, the focus is placed on the fundamental training objective to ensure broad applicability. Specifically, a novel Confidence-Uncertainty Boundary Curve (CUBC) is introduced, which establishes an explicit functional mapping between predictive confidence and uncertainty. Building upon this theoretical foundation, the Confidence-Uncertainty Boundary Loss (CUB-Loss) is proposed. This loss operates as a semantic bridge, explicitly aligning the model's uncertainty estimates with human cognitive patterns —where high confidence corresponds to low uncertainty and high error risk corresponds to high uncertainty. By imposing these directional constraints during optimization, the proposed CUB-Loss anchors the magnitude of uncertainty to prediction correctness, effectively narrowing the gap between raw model outputs and quantifiable metrics of predictive explainability. Complementing this training-time optimization, a Dual Temperature Scaling (DTS) strategy is devised to fine-tune the posterior distribution, further enhancing the calibration alignment to provide clinicians with an explicit reference for determining the acceptance of model predictions.

The main contributions of this paper are summarized as follows:

- The formulation of a Bayesian framework that utilizes VI with MC sampling to capture uncertainty. Central to this framework is the discovery of the CUBC, which establishes a theoretical mapping between confidence and uncertainty. Based on this foundation, CUB-Loss is proposed as a novel objective function that acts as an uncertainty-aware regularizer, enforcing the coupling between prediction correctness and uncertainty estimates to enhance model calibration effectively.
- The introduction of a post-hoc calibration strategy termed DTS, which employs bidirectional Temperature Scaling (TS) with two distinct temperature parameters to recalibrate the model's prediction uncertainty in opposite directions. In contrast to conventional calibration approaches, DTS increases the separability between correct and incorrect predictions in the uncertainty space without degrading classification accuracy. Together with CUB-Loss, this two-stage calibration pipeline produces well-calibrated uncertainty estimates aligned with human cognitive expectations—low for correct predictions and high for incorrect ones—thereby improving model explainability by providing clinicians with a quantitative indicator of prediction reliability.

- A comprehensive evaluation on three representative medical imaging tasks: the screening of different pneumonia types from chest radiographs [13, 14], the detection of Diabetic Retinopathy (DR) from fundus photographs [15], and the identification of skin lesions [16, 17], covering Near-Out-of-Distribution (OOD) detection, data scarcity learning, and severe class imbalance, to demonstrate the generalizability and robustness of the proposed framework.

The paper is organized as follows: Section 2 presents the techniques typically used in the state of the art for posterior inference in BNNs and the metrics commonly used, which will be utilized throughout this work; Section 3 describes the methods used and those proposed in this paper; Section 4 presents a detailed account of the experiments carried out and the results obtained in three different application domains; and finally, Section 5 draws the main conclusions of the work.

2 Related work

This section presents an overview and discusses the limitations of the most relevant approximations followed in the literature that are considered to be specifically relevant to the main objectives of this paper.

2.1 Posterior inference in Bayesian Neural Networks

Standard deterministic neural networks rely on point estimates, assigning a single fixed value to each weight parameter, which often leads to overconfident predictions. In contrast, BNNs adopt a probabilistic framework by treating model weights not as deterministic values, but as random variables governed by probability distributions. This formulation allows the model to output a predictive distribution rather than a single scalar, inherently capturing model uncertainty.

However, exact posterior inference is analytically intractable for modern, high-dimensional neural architectures. To overcome this computational bottleneck, two primary approximation strategies have emerged: MC Dropout and VI.

2.1.1 MC Dropout

MC Dropout [6] interprets dropout training as a form of approximate Bayesian inference. While computationally convenient, the approximate posterior is implicitly defined by a fixed Bernoulli dropout mask, which imposes a rigid uncertainty structure across the network and limits its capacity to capture complex posterior landscapes. Empirical studies have confirmed this limitation: Djupskås et al. [18] demonstrate that MC Dropout tends to produce uniform uncertainty across the input space, failing to capture increased uncertainty in extrapolation and interpolation regions.

Several approaches have attempted to address MC Dropout’s structural constraints at the algorithmic level. Variational Dropout [19] reinterprets Gaussian Dropout within a variational framework, enabling learnable dropout rates through the local reparameterization trick. Concrete Dropout [9] further extends this idea by employing continuous relaxations of discrete dropout masks, allowing automatic tuning of dropout probabilities during training. However, these methods remain fundamentally constrained by the dropout paradigm. Although Concrete Dropout enables automatic tuning of dropout probabilities, it parameterizes uncertainty through per-layer dropout rates rather than per-weight distributions—the posterior still operates via stochastic masking rather than continuous density estimation over weight space.

Complementary to these structural improvements, numerous post-hoc calibration methods have been proposed to recalibrate MC Dropout’s uncertainty outputs [20, 21, 22, 23]. Yet such approaches primarily operate at inference time and cannot overcome the fundamental posterior expressiveness constraints inherent to dropout-based approximations.

2.1.2 Variational Inference

In contrast, VI-based BNNs [7, 8] naturally exhibit increasing uncertainty in extrapolation regions [18], reflecting the desirable Bayesian property of appropriately decreasing certainty in data-sparse areas. This desirable behavior is enabled by VI’s capacity to place continuous distributions over weights with independently learnable mean and variance for each parameter, offering greater statistical flexibility for capturing parameter-specific uncertainty.

2.1.3 Calibration deficiencies in Variational Inference

Despite their theoretical advantages, recent research has uncovered calibration deficiencies in VI-based BNNs, which directly motivates the present work. First, VI-based BNNs exhibit degraded uncertainty calibration under distributional shift. In particular, large-scale evaluations demonstrate that VI-based BNNs often become overconfident on OOD inputs [24], a behavior attributed to approximation-induced posterior contraction rather than Bayesian inference itself [25, 26].

Moreover, the cold posterior phenomenon reveals that applying post-hoc or implicit TS can substantially improve predictive performance and uncertainty behavior in VI-trained BNNs, indicating that only the standard ELBO objective does not yield well-calibrated predictive distributions [27].

These findings suggest that VI-based BNNs require explicit and reliable calibration mechanisms.

2.2 Accuracy vs. uncertainty

Recent advances in calibration have shifted the focus from minimizing distribution-level discrepancies to explicitly optimizing the joint behavior of prediction accuracy and uncertainty. Under this paradigm, a reliable model is expected to be certain when its predictions are correct and uncertain when its predictions are wrong. This alignment ensures that the model's confidence scores serve as a reliable indicator of correctness, thereby establishing trustworthiness in safety-critical applications.

This intuition is formalized in [12] through the Accuracy vs. Uncertainty (AvU) framework. The authors proposed a taxonomy that categorizes prediction outcomes into four mutually exclusive states based on the alignment between correctness and certainty. The Accurate-Certain (AC) state represents ideal reliability where the model is both correct and certain. The Inaccurate-Uncertain (IU) state represents valid uncertainty estimation where the model erroneously predicts but appropriately signals a lack of certainty. These two states are desirable and should be maximized. Conversely, the Inaccurate-Certain (IC) state indicates high-risk behavior where the model commits errors with a high degree of certainty. The Accurate-Uncertain (AU) state reflects excessive caution where the model is correct but fails to exhibit sufficient certainty. These latter two states constitute misalignment and should be minimized during training.

Table 1 provides a summary of these four states.

Table 1: Summary of the four prediction states in the AvU framework.

State	Components
AC	Accurate + Certain
IU	Inaccurate + Uncertain
IC	Inaccurate + Certain
AU	Accurate + Uncertain

Assuming that n_{AC} , n_{AU} , n_{IC} , and n_{IU} denote the number of samples in each respective state. The AvU metric is defined as:

$$\text{AvU} = \frac{n_{AC} + n_{IU}}{n_{AC} + n_{AU} + n_{IC} + n_{IU}} \quad (1)$$

This metric directly measures the proportion of samples that exhibit dependable behavior, providing an intuitive and explainable measure of uncertainty-accuracy alignment.

To enable end-to-end optimization [12] introduced the Accuracy vs. Uncertainty Calibration (AvUC), a differentiable surrogate defined as:

$$\mathcal{L}_{\text{AvUC}} := -\log \left(\frac{n_{AC} + n_{IU}}{n_{AC} + n_{IU} + n_{AU} + n_{IC}} \right) \quad (2)$$

To make this objective differentiable, the discrete state counts are replaced with soft approximations using \tanh functions. Specifically, for each sample i with uncertainty estimate u_i and uncertainty threshold u_{th} , the soft counts are computed by weighting contributions with $\tanh(u_i)$ as a smooth indicator of uncertainty and p_i as a soft indicator of prediction correctness. The subsequent work in [28] proposed soft calibration objectives S-AvUC, which further refines this relaxation through temperature-controlled soft binning to improve optimization stability.

Despite the conceptual appeal of the AvU framework, existing optimization methods suffer from two fundamental limitations. First, the reliance on soft approximations for discrete state counts introduces a discrepancy between the surrogate objective and the actual AvU metric. The \tanh -based relaxation merely smooths the counting operation but does not alter its categorical nature.

Second, the AvU framework is inherently *state-based* rather than *distance-based*. It classifies samples into discrete categories but fails to quantify *how far* a sample deviates from a dependable configuration. Consequently, a model might achieve a high AvU score while still exhibiting suboptimal uncertainty magnitudes. For instance, two IC samples contribute equally to the loss even if one has confidence marginally above the threshold and another is severely overconfident. This categorical treatment obscures the severity of miscalibration and provides uniform gradients regardless of deviation magnitude.

Motivated by these observations, the approach proposed in this paper departs from count-based optimization of categorical states. Instead of relying on soft approximations to discrete counts, a CUBC is derived that defines the theoretical relationship between confidence and uncertainty. This geometric formulation allows a distance-based loss to be defined that directly measures how far each sample deviates from the ideal boundary, providing gradients proportional to the severity of miscalibration.

2.3 Post-hoc calibration and the limits of linear scaling

Originally proposed in [1], TS remains the most prevalent post-hoc calibration method due to its simplicity and effectiveness. Ideally, a calibrated model should minimize the Expected Calibration Error (ECE), which measures the discrepancy between predicted confidence and empirical accuracy. TS addresses this by introducing a single scalar parameter $T > 0$ to rescale the logits before the softmax function. By optimizing T to minimize the negative log-likelihood on a validation set, TS effectively aligns the confidence distribution without affecting the model's classification accuracy.

Following this success, recent research has extended the concept of calibration from confidence to predictive uncertainty. In this regard, [29] introduced the Uncertainty Calibration Error (UCE) to quantify the misalignment between estimated uncertainty and regression error, proposing that TS could also be used to calibrate uncertainty estimates. However, a critical limitation of these approaches is the implicit assumption of a simplified or linear relationship between the scaling factor and the resulting uncertainty distribution. Standard TS applies a global scaling operation that treats all samples uniformly, often neglecting the intrinsic, non-linear geometric relationship between confidence and uncertainty. The mere minimization of a scalar error metric like UCE does not guarantee that the uncertainty values respect the theoretical bounds of the probability simplex.

This work addresses this gap by explicitly modeling the calibration problem relative to the theoretical CUBC, rather than relying on the linear scaling assumption inherent in traditional UCE optimization.

3 Methodology

This section presents the key concepts of the methods used and those proposed in this paper, starting from a brief introduction to BNNs and the notation followed, followed by the theoretical definition of the CUBC, and ending with the proposed CUB-Loss and DTS strategy for post-hoc calibration.

3.1 Preliminaries: Bayesian Neural Network

Standard computer-aided decision support systems typically employ deterministic deep neural networks. These models optimize a point estimate of the weights w via the maximum likelihood estimation principle. However, this approach is fundamentally prone to overfitting and, crucially, lacks the capability to capture the uncertainty associated with the model's decisions [30, 4].

To quantify uncertainty and provide a probabilistic explainability, the objective of BNNs is to compute the predictive probability distribution $p(y|x, \mathcal{D})$ [5, 7]. This computation requires the marginalization over the posterior distribution of the weights $p(w|\mathcal{D})$:

$$p(y|x, \mathcal{D}) = \int p(y|x, w)p(w|\mathcal{D}) dw \quad (3)$$

where $p(y|x, w)$ denotes the likelihood of the prediction given specific weights, and dw indicates integration over the continuous weight space.

Given the evidence data $\mathcal{D} = \{(x, y)\}$, the prior distribution $p(w)$, and the model likelihood $p(y|x, w)$, the goal is to infer the posterior distribution over the weights $p(w|\mathcal{D})$. According to Bayes' theorem, this is formulated as:

$$p(w|\mathcal{D}) = \frac{p(y|x, w)p(w)}{\int p(y|x, w)p(w) dw} \quad (4)$$

In this equation, the numerator contains the likelihood $p(y|x, w)$ and the prior $p(w)$, while the denominator $\int p(y|x, w)p(w) dw$ represents the marginal likelihood (model evidence), which serves as a normalizing constant.

Computing the exact posterior $p(w|\mathcal{D})$ is analytically intractable due to the high-dimensional integral in the denominator [30]. Therefore, VI is used to achieve tractable approximate inference [8, 31]. In this context, VI approximates the

complex posterior $p(w|\mathcal{D})$ with a simpler variational distribution $q_\theta(w)$, parameterized by θ . The objective is to minimize the Kullback–Leibler (KL) divergence between these distributions. Note that minimizing the KL divergence is mathematically equivalent to maximizing the ELBO [7]. Consequently, the ELBO loss (negative ELBO) is minimized during training via Stochastic Gradient Descent (SGD):

$$\mathcal{L}_{\text{ELBO}} = -\mathbb{E}_{q_\theta(w)}[\log p(y|x, w)] + \text{KL}[q_\theta(w)\|p(w)] \quad (5)$$

Here, the first term $-\mathbb{E}_{q_\theta(w)}[\log p(y|x, w)]$ represents the negative expected log-likelihood (reconstruction error), encouraging data fit. The second term $\text{KL}[q_\theta(w)\|p(w)]$ acts as a regularizer, penalizing deviations of the variational distribution from the prior [31, 8].

To ensure computational tractability, the mean-field approximation is adopted, where the weights are modeled with a fully factorized Gaussian distribution [7]. Under this framework, the variational distribution $q_\theta(w)$ is parameterized by its variational parameters μ (mean) and σ (standard deviation):

$$q_\theta(w) = \mathcal{N}(w|\mu, \sigma) \quad (6)$$

The parameters μ and σ are learned iteratively by optimizing the ELBO loss.

Finally, the predictive distribution $p(y|x, \mathcal{D})$ is approximated through multiple stochastic forward passes on the network using MC estimators [7, 8]. Sampling weights w_s from the variational distribution yields:

$$p(y|x, \mathcal{D}) \approx \frac{1}{S} \sum_{s=1}^S p(y|x, w_s), \quad w_s \sim q_\theta(w) \quad (7)$$

where S denotes the number of MC samples. In practice, $p(y|x, w_s)$ corresponds to the softmax output of the network in the s -th forward pass. By averaging these outputs, this method yields a marginalized probability estimate that is robust against overfitting and enables the rigorous quantification of predictive uncertainty [32].

3.2 Theoretical definition of the Confidence-Uncertainty Boundary

In this work, the predictive entropy is adopted as the primary metric for quantifying uncertainty [12] [2] [10] [3]. Rooted in information theory, predictive entropy effectively measures the dispersion of the predictive probability distribution, thereby providing a rigorous evaluation of the model's predictive certainty [33]. All subsequent references to "uncertainty" in this work are denoted by the symbol U , which explicitly refers to the predictive entropy of the Bayesian predictive distribution.

3.2.1 Confidence and uncertainty

Based on the predictive distribution $p(y|x, \mathcal{D})$ derived in Eq. (7), let $\mathbf{p} = [p_1, \dots, p_K]$ denote the predictive probability vector over K classes, where $p_i = p(y=i|x, \mathcal{D})$.

From this vector, two key quantities are derived: the predicted class label and the associated confidence. The predicted class (\hat{y}) is defined as the index corresponding to the maximum probability:

$$\hat{y} = \underset{i \in \{1, \dots, K\}}{\operatorname{argmax}} p_i \quad (8)$$

Consequently, the confidence (\hat{p}) is defined as the probability value of the predicted class:

$$\hat{p} = \max_{i \in \{1, \dots, K\}} p_i = p_{\hat{y}} \quad (9)$$

Here, $\hat{p} \in [0, 1]$ serves as a continuous scalar representing the model's certainty regarding its decision \hat{y} .

Uncertainty (U) is quantified by the predictive entropy of the distribution \mathbf{p} [33, 12]:

$$U(\mathbf{p}) = - \sum_{i=1}^K p_i \log p_i \quad (10)$$

3.2.2 Derivation of uncertainty boundaries

A key contribution of this work is the exploration of the feasible region of uncertainty for a given confidence level. While confidence and uncertainty are generally inversely correlated, their relationship is mathematically bounded. Based on Eq. (10), the bounds U_{\min} and U_{\max} are identified by considering the behavior of prediction: when the probability mass is concentrated on fewer outcomes, the system is more ordered, and the outcomes are easier to predict, leading to a lower uncertainty. In contrast, when the distribution is more dispersed, the outcomes are harder to predict, resulting in higher entropy. Consequently, for a fixed confidence \hat{p} , the uncertainty $U(\mathbf{p})$ is strictly constrained within a theoretical range $[U_{\min}(\hat{p}), U_{\max}(\hat{p})]$.

Theoretical maximum uncertainty (U_{\max}) The uncertainty is maximized when the residual probability mass $(1 - \hat{p})$ is distributed uniformly among the remaining $K - 1$ non-target classes. This represents the state of maximum dispersion given a fixed confidence constraint. The upper bound is defined as:

$$U_{\max}(\hat{p}) = - \left[\hat{p} \log \hat{p} + \sum_{j \neq \hat{y}} \frac{1 - \hat{p}}{K - 1} \log \left(\frac{1 - \hat{p}}{K - 1} \right) \right] \quad (11)$$

where the summation runs over all indices j representing the non-target classes (i.e., $j \in \{1, \dots, K\}$ and $j \neq \hat{y}$). Since the term inside the summation is constant for all j , this expression simplifies to:

$$U_{\max}(\hat{p}) = -\hat{p} \log \hat{p} - (1 - \hat{p}) \log \left(\frac{1 - \hat{p}}{K - 1} \right) \quad (12)$$

Theoretical minimum uncertainty (U_{\min}) Conversely, the uncertainty is minimized when the residual probability mass $(1 - \hat{p})$ is concentrated entirely into a single non-target class (i.e., the second most likely class), leaving the other $K - 2$ classes with zero probability. This represents the most concentrated distribution possible for a fixed \hat{p} . The lower bound is defined as:

$$U_{\min}(\hat{p}) = - \left[\hat{p} \log \hat{p} + (1 - \hat{p}) \log(1 - \hat{p}) + \sum_{\text{others}} 0 \right] \quad (13)$$

which simplifies to:

$$U_{\min}(\hat{p}) = -\hat{p} \log \hat{p} - (1 - \hat{p}) \log(1 - \hat{p}) \quad (14)$$

The distinction between U_{\min} and U_{\max} captures qualitatively different modes of predictive uncertainty that cannot be inferred from confidence alone. When uncertainty approaches U_{\min} for a given \hat{p} , the residual probability mass of the model is concentrated on a single alternative class. This configuration indicates that the model exhibits a focused conflict between a limited number of alternatives, implying that partial exclusionary knowledge is already present. From an information-theoretic standpoint, such exclusion reduces the number of plausible outcomes and therefore lowers the uncertainty of the predictive distribution. Conversely, when the non-dominant predictions are distributed across all remaining classes without preference, the model fails to rule out any alternative hypothesis. The residual uncertainty is maximally dispersed, indicating a lack of discriminatory evidence. In this regime, additional information is required to resolve the prediction, leading to a higher uncertainty state. This configuration corresponds to the maximal achievable uncertainty for the same \hat{p} , denoted as U_{\max} .

3.2.3 Confidence-Uncertainty Boundary Curve

Based on these theoretical bounds, an ideal mapping function is represented, denoted by CUBC. A key observation motivating this representation is that in conventional BNNs, the relationship between confidence and uncertainty spans a continuous region rather than a deterministic correspondence—for any given confidence level, uncertainty can assume a range of values within the feasible bounds. This many-to-one ambiguity limits the ability to provide targeted guidance for uncertainty optimization during training. The CUBC addresses this limitation by establishing an explicit functional mapping between confidence and uncertainty, thereby enabling directional optimization that systematically steers the uncertainty distribution toward the desired calibration objectives.

Given a confidence threshold hyperparameter γ , the ideal uncertainty U_{ideal} is defined as:

$$U_{\text{ideal}}(\hat{p}) = \begin{cases} U_{\min}(\hat{p}) & \text{if } \hat{p} > \gamma \\ U_{\max}(\hat{p}) & \text{if } \hat{p} \leq \gamma \end{cases} \quad (15)$$

The geometric interpretation of this function is visually presented in Figure 1. The shaded light blue region indicates the feasible mathematical range of uncertainty $[U_{\min}, U_{\max}]$, representing all theoretically attainable confidence-uncertainty pairs. The solid blue line traces the ideal CUBC proposed (U_{ideal}) defined in Eq. (15), which collapses this region into a single-valued function that prescribes the target uncertainty for each confidence level.

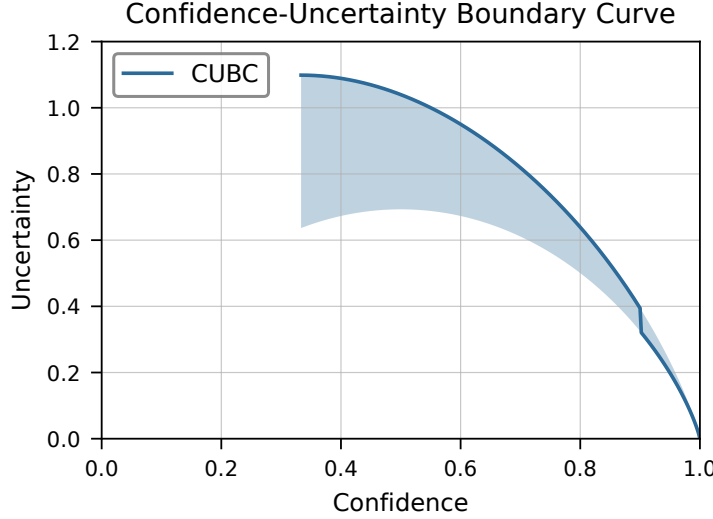


Figure 1: Visualization of the Confidence-Uncertainty Boundary Curve.

3.3 Confidence-Uncertainty Boundary Loss

Building upon the CUBC, a supervised objective named CUB-Loss is proposed. This method encourages the model to exhibit high confidence with low uncertainty for correctly predicted samples and low confidence with high uncertainty for incorrectly predicted samples, thereby achieving more calibrated and dependable model outputs.

3.3.1 Four-dimensional loss decomposition

The AvU framework [12] establishes a fundamental principle for uncertainty calibration by categorizing predictions into four quadrants according to their accuracy and uncertainty characteristics. This paradigm is extended by leveraging the explicit functional mapping provided by the CUBC. Rather than relying on soft approximations to partition samples, the proposed formulation directly computes geometric deviations from the ideal boundary curve, yielding a quantitative optimization signal that precisely steers the uncertainty distribution toward calibration targets.

Specifically, the CUBC partitions the confidence space into two regimes (high-confidence: $\hat{p} > \gamma$; low-confidence: $\hat{p} \leq \gamma$), while prediction correctness naturally divides samples into accurate ($\hat{y}_i = y_i$) and inaccurate ($\hat{y}_i \neq y_i$) categories. The Cartesian product of these two binary dimensions yields four logical regions. Region-specific deviation metrics are designed to be tailored to the optimization objective within each quadrant.

Let $\mathcal{D} = \{(x_i, y_i)\}_{i=1}^N$ denote the dataset, where N is the total number of samples. For each sample i , we denote y_i as the true label, \hat{y}_i as the predicted label, \hat{p}_i as the confidence, and U_i as the uncertainty. The boundary deviation δ_i is defined with region-dependent calculation logic:

$$\delta_i = \begin{cases} |U_{\text{ideal}}(\hat{p}_i) - U_i| & \text{if } \hat{y}_i = y_i, \hat{p}_i > \gamma \\ |\hat{p}_i - \gamma| & \text{if } \hat{y}_i = y_i, \hat{p}_i \leq \gamma \\ |\hat{p}_i - \gamma| & \text{if } \hat{y}_i \neq y_i, \hat{p}_i > \gamma \\ |U_{\text{ideal}}(\hat{p}_i) - U_i| & \text{if } \hat{y}_i \neq y_i, \hat{p}_i \leq \gamma \end{cases} \quad (16)$$

where the terms are defined as follows:

- $U_{\text{ideal}}(\hat{p}_i)$: the target uncertainty prescribed by the boundary curve for confidence \hat{p}_i .
- γ : the confidence threshold that partitions the confidence space.

The optimization objective for each region is as follows:

- Accurate-Certain ($\hat{y}_i = y_i, \hat{p}_i > \gamma$): The prediction is already in the high confidence region with the correct classification. The objective is to further minimize the uncertainty toward U_{\min} , reinforcing certain reliable predictions.
- Accurate-Uncertain ($\hat{y}_i = y_i, \hat{p}_i \leq \gamma$): The prediction is correct but remains in the low confidence region. The objective is to increase confidence toward the threshold γ , calibrating the sample into the high-confidence region.
- Inaccurate-Certain ($\hat{y}_i \neq y_i, \hat{p}_i > \gamma$): The objective is to decrease confidence toward the threshold γ , penalizing dangerous overconfident misclassifications.
- Inaccurate-Uncertain ($\hat{y}_i \neq y_i, \hat{p}_i \leq \gamma$): The objective is to increase uncertainty toward U_{\max} , encouraging the model to express high uncertainty for incorrect predictions.

This four-dimensional decomposition ensures that the optimization signal is geometrically meaningful within each region. Since the CUBC establishes an explicit mapping between confidence and uncertainty, it becomes possible to first calibrate confidence to guide predictions into the appropriate region, and subsequently refine uncertainty toward the theoretical bounds. This hierarchical calibration strategy encourages correct predictions to increase confidence while penalizing incorrect predictions that remain in the high-confidence region, systematically guiding all samples toward the ideal CUBC illustrated in Figure 1.

3.3.2 Normalization and loss formulation

For the four dimensions of the boundary deviation defined above, a linear normalization is applied, mapping them to a fixed range $[0, 1]$. This process results in the normalized deviation $\tilde{\delta}_i$, thereby ensuring that all four dimensions share a consistent numerical scale in the loss computation.

The final CUB-Loss is formulated using a logarithmic barrier function. The loss is aggregated across all samples using a direct summation to impose a heavy penalty as the normalized deviation approaches its maximum:

$$\mathcal{L}_{\text{CUB}} = \sum_{i=1}^N \left(-\log(1 - \tilde{\delta}_i) \right) \quad (17)$$

3.3.3 Joint optimization strategy

Integrating this regularization into the Bayesian framework, the total objective function combines the ELBO with the CUB-Loss:

$$\mathcal{L}_{\text{total}} = \mathcal{L}_{\text{ELBO}} + \beta \cdot \mathcal{L}_{\text{CUB}} \quad (18)$$

where $\mathcal{L}_{\text{ELBO}}$ consists of the cross-entropy loss and the KL divergence term (as defined in Eq. 5), and β is a dynamically adjusted weighting coefficient. A warm-up strategy is adopted, in which β is initially set to 0 during the early training epochs to allow the model to prioritize discriminative learning features. After the warm-up phase, β is selected by comparing the magnitude of \mathcal{L}_{CUB} with the cross-entropy and KL divergence components. Specifically, β is calculated such that the weighted term $\beta \cdot \mathcal{L}_{\text{CUB}}$ remains on the same order of magnitude as the cross-entropy and KL divergence losses. This balance strategy ensures that all three loss components contribute comparably to gradient updates, preventing any single objective from dominating the optimization process.

3.4 Dual Temperature Scaling strategy

Standard TS rescales the logits by a single scalar $T > 0$ for all samples [1]. However, as illustrated in the previous boundary analysis, the ideal relationship between confidence and uncertainty is governed by a piecewise function (U_{ideal}). A single global temperature tends to push the uncertainty of all predictions uniformly toward either the upper or lower boundary, failing to distinguish between the high-confidence/low-uncertainty regime and the low-confidence/high-uncertainty regime.

3.4.1 Definition of uncertainty calibration

To further refine the model's probabilistic outputs and align them with the discovered CUBC, a post-hoc calibration method named DTS is introduced. DTS addresses this limitation by employing two distinct temperature parameters, enabling simultaneous and bidirectional calibration of both confidence and uncertainty toward the ideal boundary curve.

Based on the CUBC derived above, the perfect uncertainty calibration is defined as:

$$U(\mathbf{p}) = U_{\text{ideal}}(\hat{p}), \quad \forall \mathbf{p} \quad (19)$$

where $\mathbf{p} = [p_1, \dots, p_K]$ denotes the predictive probability vector over K classes, $\hat{p} = \max(\mathbf{p})$ is the confidence in Eq. (9), $U(\mathbf{p})$ is the uncertainty in Eq. (10), and U_{ideal} is defined in Eq. (15). This condition requires that for any prediction, its uncertainty should equal the ideal value determined by its confidence.

To quantify the degree of calibration, a scalar summary statistic is convenient. Inspired by previous work on confidence calibration [1], uncertainty miscalibration is defined as the expectation between the predicted uncertainty and the ideal boundary:

$$\mathbb{E} [|U(\mathbf{p}) - U_{\text{ideal}}(\hat{p})|] \quad (20)$$

Boundary Curve Calibration Error (BCCE) approximates Eq. (20) by partitioning predictions into M equally-spaced bins based on confidence and taking a weighted average of the bins' uncertainty discrepancy. More precisely:

$$\text{BCCE} = \sum_{m=1}^M \frac{|B_m|}{N} |\bar{U}(B_m) - \bar{U}_{\text{ideal}}(B_m)| \quad (21)$$

where N is the total number of samples, M is the number of bins, and B_m denotes the set of indices for samples falling into the m -th bin. The terms \bar{U} and \bar{U}_{ideal} are defined as:

$$\bar{U}(B_m) = \frac{1}{|B_m|} \sum_{i \in B_m} U(\mathbf{p}_i) \quad (22)$$

$$\bar{U}_{\text{ideal}}(B_m) = \frac{1}{|B_m|} \sum_{i \in B_m} U_{\text{ideal}}(\hat{p}_i) \quad (23)$$

Here, $U(\mathbf{p}_i)$ represents the actual uncertainty calculated from the model's output distribution for sample i , and $U_{\text{ideal}}(\hat{p}_i)$ represents the target uncertainty value derived from the CUBC corresponding to the sample's confidence \hat{p}_i . The discrepancy between the model's actual uncertainty and the theoretically required uncertainty across the entire confidence spectrum is captured by this formulation.

3.4.2 The Dual Temperature Scaling algorithm

The DTS algorithm acts as a bi-directional optimization process characterized by two core properties:

- *Piecewise optimization:* It enables independent optimization of samples in high-confidence and low-confidence regimes, effectively approximating the respective segments of the CUBC.
- *Accuracy preservation:* Inherently, it maintains the rank order of logits, ensuring that the classification accuracy remains unchanged. Since TS is a monotonic transformation, it calibrates the confidence and uncertainty values without altering the rank order of the logits, thereby preserving the original classification accuracy.

A confidence threshold interval $[\gamma_{\text{low}}, \gamma_{\text{high}}]$ and an uncertainty threshold η are defined. The schematic representation of these thresholds and the resulting scaling regions is illustrated in Figure 2.

To enhance algorithmic clarity and explainability, the scaling mechanism is structured into three sequential steps:

Step 1: Distribution sharpening (T_{high})

First, samples that demonstrate high reliability are identified. The temperature T_{high} is applied to sharpen the predictive distribution (reducing $U(\mathbf{p})$ towards U_{min}) when either of the following conditions is satisfied:

- The prediction is high-confidence ($\hat{p} > \gamma_{\text{high}}$).
- The prediction falls into the intermediate confidence range with low uncertainty ($\gamma_{\text{low}} < \hat{p} \leq \gamma_{\text{high}}$ and $U(\mathbf{p}) < \eta$).

Step 2: Distribution softening (T_{low})

Second, samples that require preserved ambiguity are identified. The temperature T_{low} is applied to soften the predictive distribution (increasing $U(\mathbf{p})$ towards U_{max}) when either of the following conditions is satisfied:

- The prediction is low-confidence ($\hat{p} \leq \gamma_{\text{low}}$).

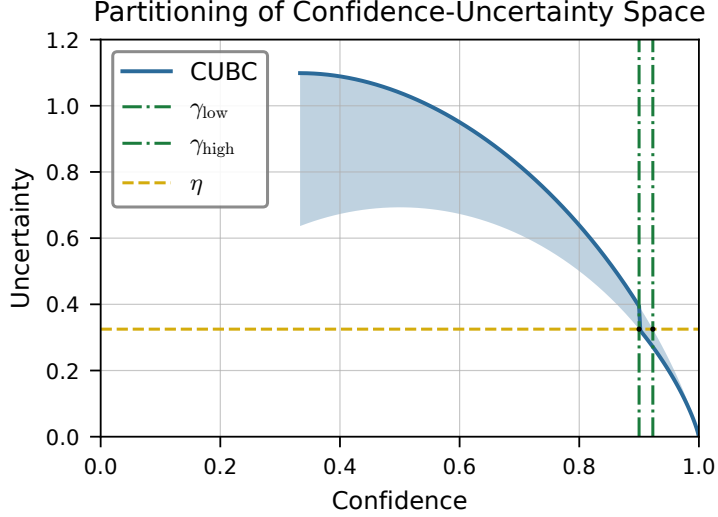


Figure 2: Partitioning of the confidence-uncertainty space by thresholds γ_{low} , γ_{high} , and η .

- The prediction falls into the intermediate confidence range with high uncertainty ($\gamma_{\text{low}} < \hat{p} \leq \gamma_{\text{high}}$ and $U(\mathbf{p}) \geq \eta$).

Step 3: Bi-directional Temperature Scaling

Given the conditions established in Steps 1 and 2, the calibrated logits $\mathbf{z}_{\text{calibrated}}$ are computed using the corresponding region-specific temperature. Let $\mathbf{z} = \frac{1}{S} \sum_{s=1}^S \mathbf{z}_s$ denote the mean logits, where \mathbf{z}_s represents the logits from the s -th MC forward pass. The scaling operation is formulated as follows.

$$\mathbf{z}_{\text{calibrated}} = \begin{cases} \mathbf{z}/T_{\text{high}} & \text{if Step 1 conditions are met} \\ \mathbf{z}/T_{\text{low}} & \text{if Step 2 conditions are met} \end{cases} \quad (24)$$

The intermediate confidence region ($\gamma_{\text{low}}, \gamma_{\text{high}}$) combined with the uncertainty threshold η introduces a transition zone that prevents abrupt scaling changes. This design enables the model to effectively distinguish between “confident-accurate” and “uncertain-inaccurate” predictions during the calibration process.

3.4.3 Optimization of temperature parameters

In post-hoc calibration methods, a hold-out validation set is typically required for calibration optimization, and this same set is also used for hyperparameter tuning [1]. Following this protocol, the optimal temperature parameters $\mathcal{T} = \{T_{\text{high}}, T_{\text{low}}\}$ are estimated on the same validation set. The optimization procedure consists of three sequential steps: (1) applying bi-directional scaling Eq. (24) to the mean logits \mathbf{z} of validation samples with candidate temperature values, (2) recalculating the predictive probability distributions and corresponding uncertainties $U(\mathbf{p})$ from the scaled logits, and (3) computing the BCCE by comparing the recalibrated uncertainties against the ideal boundary values.

With the model weights frozen, the L-BFGS optimizer is employed to minimize this calibration error.

$$\mathcal{T}^* = \underset{T_{\text{high}}, T_{\text{low}}}{\text{argmin}} \text{BCCE}(\mathcal{D}_{\text{val}}; T_{\text{high}}, T_{\text{low}}) \quad (25)$$

The resulting model exhibits a confidence-uncertainty relationship that closely approximates the ideal boundary curve, improving predictive reliability for clinical deployment.

4 Experiments

The efficacy of the proposed framework was evaluated in three distinct and challenging medical imaging tasks: screening of pneumonia types, detection of DR, and identification of skin lesions. A subsection is dedicated to each of the application domains used to evaluate the proposed methods.

This section also presents the experimental setup used to evaluate the proposed methods.

4.1 Experimental setup and evaluation

The screening of pneumonia types serves as the primary experimental testbed, where a comprehensive four-stage analysis is performed to validate each component of the proposed method rigorously.

1. First, a VI-based BNNs is established as a baseline to represent standard probabilistic modeling.
2. Second, the proposed learning with CUB-Loss is integrated into the Bayesian training process to assess its impact on intrinsic calibration.
3. Third, the post-hoc DTS mechanism, optimized via the BCCE metric, is applied to the CUB-Loss-trained model to demonstrate the benefits of the complete calibration pipeline.
4. Finally, the robustness of the model is evaluated by testing with the OOD dataset to ensure reliability in open-world settings.

To verify the universality and generalizability of the proposed method, the evaluation is extended to the detection of DR and the identification of skin lesions. For these additional datasets, a streamlined protocol is adopted that focuses on a comparative analysis between the baseline Bayesian model and the model enhanced with the proposed CUB-Loss mechanism. This design allows consistent performance gains to be demonstrated across different clinical domains without redundant ablation steps.

4.1.1 Evaluation metrics

To quantitatively assess model performance, standard classification accuracy is employed to measure predictive correctness, and the AvU metric [12] is used to evaluate the alignment between model confidence and reliability. In addition, a detailed statistical analysis of the output uncertainty values and their distributions is conducted. This analysis verifies whether the model successfully assigns lower uncertainty to correct predictions and higher uncertainty to incorrect ones, adhering to the principles of dependable clinical decision-making.

For the OOD detection task, the problem is modeled as a binary classification task that distinguishes between In-Distribution (ID) and OOD samples based on their predictive uncertainty. Following the evaluation protocol established in prior work [34], two widely used metrics are employed: the Area Under the Receiver Operating Characteristic Curve (AUROC) and the Area Under the Precision-Recall Curve (AUPR). AUROC measures the probability that a randomly chosen OOD sample receives a higher anomaly score than a randomly chosen ID sample, while AUPR summarizes the precision-recall trade-off across varying thresholds. Higher values in both metrics indicate that the model assigns consistently higher uncertainty scores to OOD samples compared to ID samples, effectively flagging them as “unknown” to prevent silent failures.

4.2 Experiment 1: screening of pneumonia types from chest X-ray images

Chest radiography is a vital complementary modality for the screening of pneumonia and the detection of its specific etiology: viral, bacterial, or fungal [35]. Although deep learning approaches have demonstrated remarkable potential in automating the analysis of X-ray images for this purpose [36], a potential clinical deployment requires more than just high classification accuracy in known categories.

4.2.1 Datasets

Beyond accurate classification of known categories, a clinically reliable screening system must also identify inputs that fall outside its learned distribution [37]. This capability is essential for detecting “silent failures” where the model might otherwise produce overconfident but erroneous predictions on unfamiliar pathologies.

Thus, classification performance is evaluated on ID data, and reliability is subsequently assessed by rejecting samples from an OOD dataset.

In-Distribution dataset The ID dataset was compiled by aggregating data from multiple publicly available repositories to create a large-scale, balanced corpus. This dataset comprises over 56,000 posterior-anterior and anterior-posterior chest radiographs, categorized into three classes: Pneumonia (non-COVID-19 viral, bacterial, or fungal), COVID-19, and Control (no findings). The corpus was randomly partitioned into training, validation, and test subsets with a ratio of 70:15:15, using stratified splitting to preserve the class distribution. The detailed distribution is presented in Table 2.

The pneumonia class was compiled by combining samples from MIMIC-CXR [38] and CheXpert [14] to enhance intra-class variability and introduce realistic clinical complexity.

Table 2: Distribution of In-Distribution datasets.

Subset	Pneumonia	COVID-19	Control	Total
Train	10,676	13,999	14,905	39,580
Validation	2,287	2,999	3,193	8,479
Test	2,290	2,999	3,194	8,483
Total	15,253	19,997	21,292	56,542

The COVID-19 class was curated from the COVIDx CXR-4 dataset [39], which consolidates imaging data from multiple repositories including the COVID-19 Chest X-ray dataset [40], Actualmed COVID-19 Chest X-ray dataset [41], COVID-19 Radiography database [42], RSNA International COVID-19 Open Radiology database [43], BIMCV-COVID19+ [44], and Stony Brook University COVID-19 Positive Cases [45]. From this consolidated corpus, approximately 20,000 COVID-19 positive images were selected.

The control class was sourced from the NIH ChestX-ray14 dataset [13], strictly selecting images labeled as “No Finding” to minimize label noise and clinical ambiguity.

Out-of-Distribution dataset A Near-OOD test set was constructed from the NIH ChestX-ray14 dataset [13]. Unlike standard Far-OOD benchmarks that utilize semantically distinct natural images, the evaluation focuses on the more challenging task of distinguishing between clinically distinct thoracic pathologies within the same imaging domain.

This setup presents high complexity because the OOD samples share identical anatomical structure and grayscale imaging characteristics with the ID data. Five pathology categories (Pneumothorax, Emphysema, Fibrosis, Nodule/Mass, and Atelectasis), characterized by structural deformations or chronic tissue alterations, exhibit radiological patterns with minimal overlap in imaging appearance compared to pneumonia and COVID-19. The composition is detailed in Table 3.

Table 3: Composition of the Near-OOD test set.

Pathology Category	Sample Count
Pneumothorax	1,457
Emphysema	1,457
Fibrosis	1,215
Nodule / Mass	2,914
Atelectasis	1,457
Total OOD Samples	8,500

4.2.2 Model architecture and training

The foundation of the screening system developed is the COVID-Net-Large architecture proposed in [39].

This specialized architecture was selected because it utilizes a lightweight projection-expansion-projection-extension design pattern explicitly tailored for chest radiography. This domain-specific design offers superior feature extraction capabilities for thoracic pathology compared to general-purpose models adapted via transfer learning.

This architecture was adapted to create the BCXR-Net.

BCXR-Net To adapt the architecture, the classification head was first modified, which consists of three fully connected layers. Dropout regularization with a rate of 0.2 was incorporated after the first two fully connected layers (before the final classifier layer) to provide complementary regularization for improved generalization. The modified network was then converted into a Bayesian variant, denoted as BCXR-Net, by replacing standard convolutional and linear layers with their Bayesian counterparts using the reparameterization trick [7]. By treating the weights as random variables sampled from learned distributions rather than point estimates, this architecture enables the direct integration of uncertainty quantification into the forward pass [46].

Integration of Confidence-Uncertainty Boundary Loss To further enhance the discriminative capability of the model’s uncertainty estimates, the proposed CUB-Loss is integrated into the Bayesian framework. The total objective

function defined in Eq. (18) is optimized. Following the joint optimization strategy described in Section 3.3.3, a warm-up strategy is employed in which β is set to 0 for the first 5 epochs and then fixed at 0.1 for the remaining training epochs. For the specific configuration of the CUB-Loss, the confidence threshold is set to $\gamma = 0.9$, which corresponds to a theoretical uncertainty lower bound of approximately 0.325.

Training protocol and hyperparameters The experiment was implemented using the PyTorch framework. All experiments were conducted with a fixed random seed of 42 to ensure reproducibility.

For preprocessing, input images were resized to 256 pixels on the shorter side and then center-cropped to 240×240 pixels. Although the original chest radiographs are grayscale, the images were processed as 3-channel RGB input by replicating the single intensity channel. This strategy maintains architectural compatibility with backbones pre-trained on general-purpose color datasets, thereby preserving the flexibility to leverage transfer learning. All images were normalized using standard ImageNet statistics (mean = [0.485, 0.456, 0.406], std = [0.229, 0.224, 0.225]) for each channel. Data augmentation was applied during training to improve generalization, including random resized cropping (scale range 0.5–1.0) and random horizontal flipping.

The network was trained using the SGD optimizer with a momentum of 0.9 and a weight decay of 5×10^{-4} . A cosine annealing learning rate schedule was employed to smoothly decay the learning rate from an initial value of 4×10^{-4} over 50 epochs with a batch size of 128.

For the stochastic variational layers, 5 MC samples per forward pass were utilized during training to balance computational efficiency with gradient estimation accuracy, while 80 MC forward passes were used during inference to obtain robust probability estimates and uncertainty quantification.

Post-hoc calibration protocol After training, the DTS mechanism described in Section 3.4 was applied to recalibrate the model’s probabilistic outputs. The calibration was performed on the held-out validation set with frozen model weights to prevent data leakage.

The uncertainty threshold was set to $\eta = 0.325$, and the corresponding confidence thresholds $\gamma_{\text{low}} = 0.9$ and $\gamma_{\text{high}} = 0.923$ were derived from the ideal boundary curve at this uncertainty level. The optimal temperature parameters $\mathcal{T} = \{T_{\text{high}}, T_{\text{low}}\}$ were determined by minimizing the BCCE using the L-BFGS optimizer with a learning rate of 0.01 and a maximum of 50 iterations.

4.2.3 Experimental results

The results are presented separately for the ID and OOD datasets.

In-Distribution Classification and Calibration To evaluate the contribution of each proposed component, four configurations were compared: the baseline Bayesian model (BCXR-Net); BCXR-Net with $\mathcal{L}_{\text{AvUC}}$ [12]; BCXR-Net with the proposed \mathcal{L}_{CUB} ; and BCXR-Net with \mathcal{L}_{CUB} combined with DTS. All experiments were performed with identical hyperparameters to ensure a fair comparison. To quantify the calibration effectiveness, the uncertainty separation metric $\Delta U = \bar{U}_{\text{incorrect}} - \bar{U}_{\text{correct}}$ is introduced, which measures the difference in mean uncertainty between incorrect and correct predictions. A higher ΔU indicates that the model assigns high uncertainty to erroneous predictions and low uncertainty to correct ones, thereby reflecting better calibration quality.

Table 4: Classification and calibration results using the ID dataset.

Method	Acc. (%) \uparrow	AvU \uparrow	$\Delta U \uparrow$
BCXR-Net (Baseline)	95	0.43	0.26
+ $\mathcal{L}_{\text{AvUC}}$	84	0.59	0.32
+ \mathcal{L}_{CUB}	97	0.90	0.45
+ \mathcal{L}_{CUB} + DTS	97	0.95	0.58

Table 4 summarizes the experimental results. The baseline Bayesian model achieves an accuracy of 95% with an AvU of 0.43. Adding $\mathcal{L}_{\text{AvUC}}$ improves the AvU score to 0.59 but lowers the accuracy. In contrast, the proposed \mathcal{L}_{CUB} achieves higher accuracy (97%) and improved AvU (0.90), demonstrating more effective regularization for uncertainty calibration. The uncertainty separation ΔU increases from 0.26 (baseline) to 0.58 (complete framework), representing a substantial improvement. This enhanced separation is critical for clinical deployment, where reliable uncertainty estimates enable the identification of predictions requiring expert review.

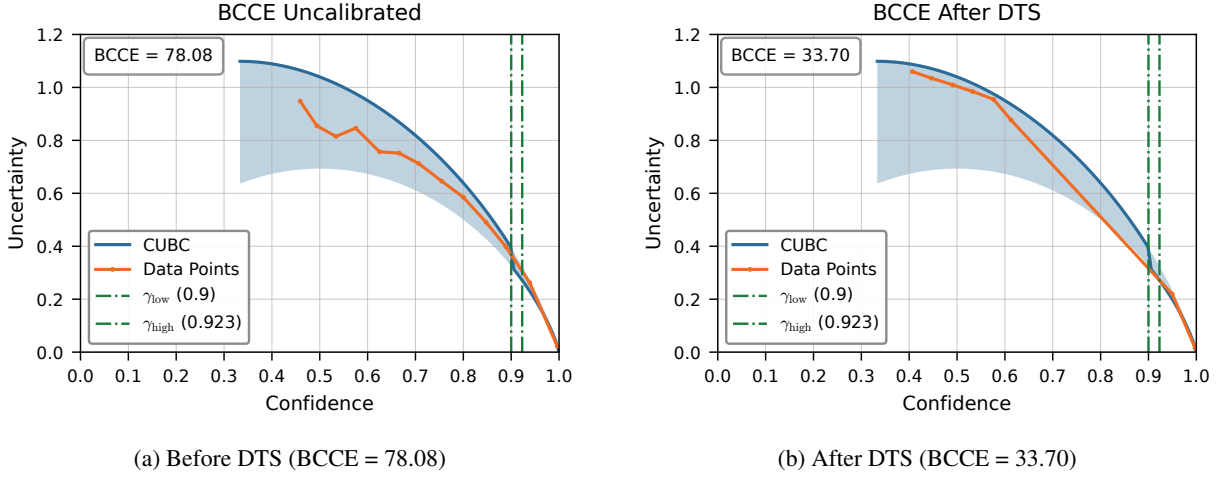


Figure 3: Boundary Curve Calibration Error before DTS (a) and after DTS (b).

Figure 3 illustrates the effect of DTS on the confidence-uncertainty relationship. Before calibration, the empirical curve deviates substantially from the theoretical boundary, particularly in the low-to-medium confidence region. The optimal temperature parameters ($T_{\text{high}} = 0.874$, $T_{\text{low}} = 2.991$) were obtained by minimizing BCCE on the validation set using the L-BFGS optimizer. After applying DTS with these optimized temperatures, the empirical curve aligns closely with the theoretical bound, with BCCE reduced from 78.08 to 33.70 (a 56.8% reduction). This calibration improvement is achieved without affecting classification accuracy, as TS preserves the rank order of predictions. These results demonstrate that \mathcal{L}_{CUB} provides effective training-time regularization for uncertainty calibration, while DTS offers complementary post-hoc refinement. Together, they yield a well-calibrated uncertainty-aware screening system suitable for clinical deployment.

Out-of-Distribution detection OOD detection is formulated as a binary classification problem using a scoring function that assigns each sample a value indicating its likelihood of being ID or OOD [34]. Unlike standard Far-OOD benchmarks that utilize semantically distinct natural images [47], the Near-OOD evaluation presents a significantly more challenging scenario. The OOD samples in the test set share identical anatomical structures and grayscale imaging characteristics with ID data, differing only in subtle pathological patterns that occupy a small fraction of the image area.

Based on the BCXR-Net model, the proposed method was compared with several established OOD detection approaches. For output-based methods, the maximum softmax probability (confidence) was employed as the scoring function [48]; in contrast, uncertainty was utilized as the primary indicator in the proposed method [49]. Regarding feature-based methods, the Mahalanobis distance and Relative Mahalanobis distance with single-layer and multi-layer feature fusion were evaluated [50]. Additionally, Relative Mahalanobis combined with input perturbation was examined [51]. Kernel Principal Component Analysis (PCA) variants that exploit non-linear mappings were also evaluated [52]: in Cosine + PCA, cosine normalization is applied prior to dimensionality reduction, whereas in Cosine + Random Fourier Features (RFF) + PCA, RFF is employed to approximate Gaussian kernels for enhanced OOD separability.

Table 5 presents the OOD detection results. The moderate overall performance across all methods reflects the inherent difficulty of Near-OOD detection in medical imaging [47, 50], where discriminative lesion regions occupy only a small portion of the image area [37]. The proposed calibrated uncertainty (BCXR-Net + \mathcal{L}_{CUB} + DTS) achieves the best performance with an AUROC of 74.2% and AUPR of 79.4%, outperforming both output-based baselines and feature-based alternatives. These results demonstrate that the proposed framework provides meaningful OOD detection capability even in the challenging Near-OOD regime, enhancing both ID classification reliability and the identification of out-of-scope inputs.

4.3 Experiment 2: diabetic retinopathy detection

DR represents a critical microvascular sequela of diabetes mellitus and persists as a leading cause of preventable blindness among the working-age population globally. Although fundus photography constitutes the primary detection modality, manual grading relies heavily on subjective expert interpretation.

Table 5: Results on the Near-OOD test set.

Method	AUROC \uparrow	AUPR \uparrow
<i>Output-based methods</i>		
\mathcal{L}_{CUB} (confidence)	71.1	73.7
\mathcal{L}_{CUB} (uncertainty)	71.1	73.7
$\mathcal{L}_{\text{CUB}} + \text{DTS}$ (confidence)	73.9	78.7
$\mathcal{L}_{\text{CUB}} + \text{DTS}$ (uncertainty)	74.2	79.4
<i>Feature-based methods</i>		
Mahalanobis	61.2	68.9
Relative Mahalanobis (single-layer)	62.3	69.4
Relative Mahalanobis (multi-layer)	64.0	71.9
Relative Mahalanobis + perturbation	63.9	71.8
Cosine + PCA	59.0	68.6
Cosine + RFF + PCA	65.0	72.6

While widespread research has focused on deploying deep learning algorithms to automate this detection process, reliable implementation faces substantial challenges, particularly due to the varying quality of fundus images and the presence of ambiguous lesions. In such high-stakes clinical environments, standard deterministic models often fail to account for these uncertainties, potentially leading to overconfident prediction. Consequently, the integration of robust uncertainty estimation mechanisms is essential to ensure that automated systems can safely flag uncertainty samples for human review [53].

4.3.1 Dataset

To evaluate the generalization capability of the proposed framework in the domain of retinal imaging, the APTOS 2019 Blindness Detection dataset [54] was utilized. Specifically, a preprocessed derivation of this corpus [55] was employed, in which all images were resized to a uniform dimension of 224×224 pixels and underwent Gaussian filtering to reduce high-frequency noise and lighting artifacts. The dataset comprises 3,662 retinal fundus images categorized into five severity levels: No DR (level 0), Mild DR (level 1), Moderate DR (level 2), Severe DR (level 3), and Proliferative DR (level 4). As shown in Table 6, the dataset exhibits significant class imbalance, with the majority of samples belonging to the No DR category.

Table 6: Distribution of fundus images across the five severity grades for the diabetic retinopathy dataset.

Subset	No DR	Mild	Moderate	Severe	Proliferative	Total
Train	1,444	296	799	155	235	2,929
Validation	180	37	100	19	30	366
Test	181	37	100	19	30	367
Total	1,805	370	999	193	295	3,662

4.3.2 Experimental configurations for robustness evaluation

The predictive uncertainty quantified in BNNs comprises both aleatoric and epistemic components. Aleatoric uncertainty arises from inherent noise in the data, such as image quality variations and ambiguous lesion boundaries, which cannot be reduced by collecting more data. Epistemic uncertainty, in contrast, stems from insufficient knowledge due to limited training data or model capacity, and is theoretically reducible by observing more data or increasing model capacity [56].

Since the same dataset is utilized with only the sample size varying while other factors remain constant, the observed differences in uncertainty across configurations primarily reflect changes in epistemic uncertainty, as the aleatoric component is inherent to the data distribution and thus theoretically invariant.

To evaluate the robustness of the proposed \mathcal{L}_{CUB} under realistic deployment conditions and analyze its behavior under varying levels of epistemic uncertainty, experiments were conducted using the following data configurations:

- Full dataset (100%): the original dataset with inherent class imbalance, partitioned into training, validation, and test subsets using a stratified split of 80:10:10.

- Reduced train/val (50%): only 50% of the original training and validation samples are randomly retained, while the test set remains identical to that of the full dataset. Class proportions are preserved within the reduced subsets.
- Reduced train/val (25%): only 25% of the original training and validation samples are retained under the same protocol, representing an extreme data scarcity scenario with a fixed test distribution.
- Balanced (train/val): the original test set is isolated first to preserve the natural class distribution for unbiased evaluation. The training and validation sets are then balanced via data augmentation applied only to minority classes.

4.3.3 Model architecture and training

For this experiment, the ResNet-34 architecture was chosen as the deterministic backbone. This selection is substantiated by extensive comparative analyses in the literature. As demonstrated in [57], ResNet architectures consistently outperform shallower networks in DR detection by effectively mitigating the vanishing gradient problem through residual skip connections. This depth is crucial to capture the details necessary to identify early-stage DR lesions. Furthermore, studies on transfer learning for medical imaging [15, 58] highlight that ResNet variants pre-trained on ImageNet possess robust feature extraction capabilities that generalize exceptionally well to retinal fundus images [59].

BResNet-34 To adapt the architecture for the DR severity grading task, the original fully connected layer was replaced with a custom classification head. The modified head consists of a linear layer reducing the 512-dimensional feature vector to 128 dimensions, followed by a ReLU activation and dropout regularization (rate = 0.1) for overfitting prevention, and a final linear layer mapping to the output classes.

To ensure methodological consistency and rigorously evaluate the generalizability of the proposed framework, the same Bayesian construction protocol established in Experiment 1 was followed, converting the modified ResNet-34 into a BNN version (BResNet-34) by replacing standard convolutional and linear layers with their Bayesian counterparts using the reparameterization trick.

Training protocol and hyperparameters The experiments were implemented using the PyTorch framework. All experiments were conducted with a fixed random seed of 42 to ensure reproducibility.

For preprocessing, retinal fundus images were normalized using standard ImageNet statistics (mean = [0.485, 0.456, 0.406], std = [0.229, 0.224, 0.225]) for each channel. Data augmentation was applied during training, including random horizontal flipping (probability = 0.5), random rotation (up to 10 degrees), and color jittering (brightness and contrast variation of 0.1). During validation and testing, only normalization was applied without augmentation.

Unlike Experiment 1, which employed direct Bayesian training, a two-stage training strategy was adopted to facilitate stable convergence. In the first stage, the deterministic ResNet-34 initialized with ImageNet pre-trained weights was fine-tuned until convergence using standard cross-entropy loss. For the deterministic ResNet-34 training stage, the model was trained using the SGD optimizer with a batch size of 32, a learning rate of 0.05, and trained for 40 epochs. In the second stage, the converged model was converted to BResNet by replacing standard convolutional and linear layers with their Bayesian counterparts. The learned weights from the first stage were used to initialize the mean of the variational posterior distributions, providing a stable starting point that accelerates convergence and enables \mathcal{L}_{CUB} to focus on uncertainty calibration rather than basic feature learning.

After the Bayesian conversion, the BResNet was trained using the total objective function defined in Eq. (18), which combines the VI objective $\mathcal{L}_{\text{ELBO}}$ with the proposed uncertainty calibration loss \mathcal{L}_{CUB} . To further stabilize uncertainty-aware optimization, a warm-up strategy was employed where β was set to 0 for the first 5 epochs and then fixed at 1.2 for the remaining training epochs. The confidence threshold was set to $\gamma = 0.9$, corresponding to a theoretical uncertainty lower bound of approximately 0.325.

The network was trained using the SGD optimizer with a momentum of 0.9 and a weight decay of 5×10^{-4} . A cosine annealing learning rate schedule was employed to smoothly decay the learning rate from an initial value of 4×10^{-4} over 80 epochs with a batch size of 16. For the stochastic variational layers, 5 MC samples per forward pass were utilized during training to balance computational efficiency with gradient estimation accuracy, while 80 MC forward passes were used during inference for robust uncertainty quantification.

4.3.4 Experimental results

Table 7 and Table 8 summarize the classification performance and uncertainty estimates under different training/validation data configurations with a fixed test distribution.

Table 7: Diabetic retinopathy classification results.

Data Configuration	BResNet		+ \mathcal{L}_{CUB}	
	Acc. (%)	AvU	Acc. (%)	AvU
Reduced train/val (25%)	70	0.68	76	0.76
Reduced train/val (50%)	74	0.70	79	0.73
Full dataset	80	0.68	81	0.76
Balanced (train/val)	82	0.61	82	0.79

Table 8: Mean uncertainty for correct and incorrect predictions under different data configurations.

Data Configuration	BResNet		+ \mathcal{L}_{CUB}	
	U_{correct}	$U_{\text{incorrect}}$	U_{correct}	$U_{\text{incorrect}}$
Reduced Train/Val (25%)	0.56	1.20	0.26	0.82
Reduced Train/Val (50%)	0.48	1.14	0.26	0.81
Full Dataset (100%)	0.34	0.85	0.19	0.65
Balanced (Train/Val)	0.46	1.01	0.16	0.56

As shown in Table 7, the proposed \mathcal{L}_{CUB} improves both classification accuracy and uncertainty calibration across all settings. Under the balanced (train/val) configuration where both models achieve identical accuracy (82%), \mathcal{L}_{CUB} yields a substantially higher AvU (0.79 vs 0.61), demonstrating that the calibration improvement is independent of accuracy gains.

Unlike Experiment 1, where the abundant training data and balanced class distribution effectively reduce epistemic uncertainty affection, making ΔU a fair metric for comparing prediction performance, Experiment 2 does not adopt this metric. Due to the limited availability and class imbalance in this dataset, the baseline BResNet exhibits sensitivity to epistemic uncertainty, resulting in uncalibrated uncertainty outputs. Under such conditions, the ΔU comparison becomes unreliable.

Instead, the analysis focuses on demonstrating the robustness of \mathcal{L}_{CUB} under elevated epistemic uncertainty. Under severe data scarcity (25% training data), the baseline BResNet exhibits substantially increased uncertainty for both correct and incorrect predictions, indicating high sensitivity to epistemic uncertainty arising from limited training data. In contrast, \mathcal{L}_{CUB} not only maintains higher accuracy (76% vs 70%) but also preserves stable uncertainty estimates, with U_{correct} remaining consistently low across all configurations. According to the definition of epistemic uncertainty, this ability to maintain calibration under data scarcity demonstrates that \mathcal{L}_{CUB} effectively reduces the impact of epistemic uncertainty, indicating stronger model capability.

The balanced configuration further validates this finding. Data balancing through augmentation effectively increases the amount of training data for minority classes, thereby reducing epistemic uncertainty. Under this configuration, \mathcal{L}_{CUB} achieves the lowest uncertainty for both correct predictions ($U_{\text{correct}} = 0.16$) and incorrect predictions ($U_{\text{incorrect}} = 0.56$) across all settings, demonstrating that the proposed method can fully leverage the reduced epistemic uncertainty from data augmentation to achieve optimal calibration performance.

These results demonstrate that the proposed \mathcal{L}_{CUB} effectively enhances the calibration capability of BNNs, providing more robust uncertainty estimates in data-scarce scenarios by mitigating the impact of epistemic uncertainty arising from limited training data.

4.4 Experiment 3: identification of skin lesions

The visual differentiation between malignant melanomas and benign pigmented lesions is challenging even for experienced dermatologists due to high inter-class similarity and visual complexity. While deep learning has shown promise in automating this process, the severe class imbalance in real-world dermatological data poses a significant risk of model bias. Therefore, calibration mechanisms that can accurately quantify the uncertainty for underrepresented classes are essential for a reliable clinical decision. [60]

4.4.1 Dataset

The proposed method was evaluated using the Human Against Machine with 10000 Training Images (HAM10000) dataset [16], a large-scale collection of multi-source dermatoscopic images of common pigmented skin lesions. The original dataset contains multiple images of the same lesion captured at different magnifications or angles. To ensure a rigorous evaluation and prevent data leakage between training and testing sets, a cleaning procedure was performed to remove duplicate entries derived from the same lesion identifier. This resulted in a refined corpus of 7,470 unique dermatoscopic images.

The dataset contains seven different categories: Melanocytic nevi (NV), Melanoma (MEL), Benign keratosis-like lesions (BKL), Basal cell carcinoma (BCC), Actinic keratoses (AKIEC), Vascular lesions (VASC), and Dermatofibroma (DF). As illustrated in the distribution statistics, the data exhibit extreme class imbalance; the majority class (NV) accounts for approximately 72.3% of the total dataset (5,403 images), whereas rare classes like DF contain as few as 73 images.

A stratified splitting strategy was followed to partition the dataset into training, validation, and test subsets with a ratio of 80:10:10. This ensures that the distinct relative proportions of each category are preserved across all folds. The specific distribution of the images per class and subset is detailed in Table 9.

Table 9: Distribution of skin lesions across the seven categories in the HAM10000 dataset.

Dataset Category	Train	Validation	Test	Total
NV	4,322	540	541	5,403
BKL	581	72	74	727
MEL	491	61	62	614
BCC	261	32	34	327
AKIEC	182	22	24	228
VASC	78	9	11	98
DF	58	7	8	73
Total	5,973	743	754	7,470

4.4.2 Model architecture and training

For this experiment, the ResNet-50 architecture was chosen as the deterministic backbone. According to the systematic review by [17], ResNet-50 offers a favorable trade-off between computational complexity and predictive performance for the identification of skin lesions, making it a particularly suitable choice for this task compared with alternative backbone architectures.

BResNet-50 The architecture for the seven-class skin lesion classification task was adapted, replacing the original fully connected layer with a custom classification head consisting of a linear layer reducing the 2048-dimensional feature vector to 512 dimensions, followed by a ReLU activation and dropout regularization (rate = 0.3), and a final linear layer mapping to the seven output classes.

Following the same protocol established in previous experiments, the modified ResNet-50 was converted into a BNN version (BResNet-50) by replacing standard convolutional and linear layers with their Bayesian counterparts.

Training protocol and hyperparameters The experiments were carried out using the PyTorch framework with a fixed random seed of 42 to ensure reproducibility.

Given the severe class imbalance in the HAM10000 dataset, class-weighted cross-entropy loss was employed during both the deterministic ResNet-50 pre-training stage and the subsequent Bayesian stage with the combined loss defined in Eq. (18). Specifically, class weights were computed using the balanced weighting scheme, ensuring that minority classes contributed proportionally more to the loss function. This strategy prevents the model from being biased toward majority classes and ensures a fair comparison between deterministic and Bayesian variants.

A two-stage training strategy similar to the one in Experiment 2 was adopted. For training the deterministic ResNet-50, the Adam optimizer was used with a batch size of 64, a learning rate of 1×10^{-3} , and a weight decay of 1×10^{-4} . Early stopping based on validation loss was employed with a patience of 50 epochs to prevent overfitting.

However, unlike Experiments 1 and 2, the Model Priors with Empirical Bayes using Deterministic Neural Networks (MOPED) initialization strategy [61, 62] is adopted for the Bayesian network. Specifically, the prior mean is set to the

pre-trained weights w_{MLE} , anchoring the prior distribution at a plausible solution obtained from deterministic training. The variational posterior is initialized with mean $\mu_q = w_{\text{MLE}}$ and a scale parameterized by $\rho = \log(\exp(\alpha|w_{\text{MLE}}|) - 1)$ with $\alpha = 0.01$, providing a controlled initial uncertainty proportional to the magnitude of the pre-trained weights.

After MOPED-based initialization, the model was trained using the same total objective as in Experiments 1 and 2, namely the combined loss defined in Eq. (18), which integrates the VI objective $\mathcal{L}_{\text{ELBO}}$ with the proposed uncertainty calibration loss \mathcal{L}_{CUB} .

This empirical Bayes initialization offers a principled warm-start for Bayesian transfer learning, yielding informative priors while maintaining stable optimization dynamics. Such initialization is particularly advantageous in severely imbalanced datasets, where anchoring the posterior around a meaningful solution can improve training stability and mitigate premature convergence toward majority-class-dominated predictions.

The network was trained using the SGD optimizer with a momentum of 0.9 and weight decay of 5×10^{-4} . The learning rate was set to 1×10^{-3} with a batch size of 64. Following the same approach as in previous experiments, a warm-up strategy was employed where β was set to 0 for the first 30 epochs, then fixed at 0.6 for the remaining epochs. The extended warm-up period allows the model to adapt to the informative priors before introducing uncertainty calibration. The confidence threshold was set to $\gamma = 0.9$, corresponding to a theoretical uncertainty lower bound of approximately 0.325.

Given the severe class imbalance in the HAM10000 dataset, Balanced Accuracy (BACC) was employed as monitoring metric for early stopping. Training was finished if BACC had no improvements for 15 consecutive epochs after the introduction of \mathcal{L}_{CUB} , preventing overfitting while ensuring sufficient calibration refinement. For inference, 80 MC forward passes were used for robust uncertainty quantification.

4.4.3 Experimental results

Table 10: Results on the identification of skin lesions using the HAM10000 dataset.

Method	Acc. (%)	BACC (%)	AvU
ResNet-50 (Deterministic)	84	69	–
BResNet-50 (Baseline)	81	64	0.79
BResNet-50 + \mathcal{L}_{CUB} (Ours)	85	66	0.84

Table 10 presents the results on the HAM10000 dataset. BNNs typically struggle with severely imbalanced data, as evidenced by the performance drop from the deterministic ResNet-50 (BACC 69%) to the BResNet-50 baseline (BACC 64%). Incorporating \mathcal{L}_{CUB} partially recovers this gap (BACC 66%) while substantially improving uncertainty calibration (AvU: 0.79 → 0.84). Although BACC remains below the deterministic baseline, the model achieves higher AvU, indicating that predictions on difficult minority-class samples are appropriately flagged as uncertain rather than overconfidently misclassified. This demonstrates that \mathcal{L}_{CUB} can extend the applicability of Bayesian models to challenging imbalanced scenarios where they would otherwise underperform.

5 Conclusions

This paper presents a unified framework for uncertainty calibration in BNNs for medical image classification, comprising two complementary components: the CUB-Loss (\mathcal{L}_{CUB}) for training-time calibration and DTS for post-hoc refinement.

We validated the proposed framework across three distinct medical imaging tasks with varying characteristics. In Experiment 1 (screening of pneumonia types), the complete framework achieved 97% accuracy with an AvU of 0.95. It demonstrated an effective Near-OOD detection capability (AUROC of 74.2%), outperforming both output-based and feature-based alternatives. In Experiment 2 (DR detection), we evaluated robustness under conditions of data scarcity and class imbalance. The results showed that \mathcal{L}_{CUB} provides implicit regularization, maintaining higher accuracy and a more stable AvU even when the training data was reduced to 25%. Notably, under the balanced (train/val) configuration where accuracy remained constant, AvU improved from 0.61 to 0.79, confirming that calibration gains are independent of accuracy improvements. In Experiment 3 (identification of skin lesions), we addressed the challenge of applying Bayesian models to severely imbalanced data. Using MOPED initialization combined with \mathcal{L}_{CUB} , the framework recovered performance degradation typically observed in Bayesian conversion (BACC: 64% → 66%) while achieving improved uncertainty calibration (AvU: 0.79 → 0.84).

As observed in our experiments, BNNs can face optimization challenges under limited data (Experiment 2) and severe class imbalance (Experiment 3). Our results demonstrate that \mathcal{L}_{CUB} is compatible with different Bayesian

training strategies, including two-stage training with posterior initialization and MOPED with informative priors [61], consistently improving uncertainty calibration across these challenging scenarios. While the choice of initialization strategy depends on specific data characteristics, the consistent calibration improvements achieved by \mathcal{L}_{CUB} across all settings suggest its general applicability.

In summary, the proposed framework provides a principled and generalizable approach to uncertainty-aware medical image classification, extending the practical applicability of BNNs to challenging real-world clinical scenarios and significantly improving the explainability of the underlying models.

Data and code availability

All datasets used in this study are publicly available:

- Pneumonia screening: compiled from MIMIC-CXR (<https://physionet.org/content/mimic-cxr/2.1.0/>), CheXpert (<https://stanfordaimi.azurewebsites.net/datasets/8cbd9ed4-2eb9-4565-affc-111cf4f7ebe2>), COVIDx CXR-2 (<https://www.kaggle.com/datasets/andyczhao/covidx-cxr2>), and NIH Chest X-rays (<https://www.kaggle.com/datasets/nih-chest-xrays/data>). Dataset construction details are described in the paper.
- Diabetic retinopathy detection: preprocessed dataset available at <https://www.kaggle.com/datasets/sovitrath/diabetic-retinopathy-224x224-gaussian-filtered>, derived from the APTOS 2019 Blindness Detection challenge.
- Identification of skin lesions: available at <https://www.kaggle.com/datasets/kmader/skin-cancer-mnist-ham10000>.

The code is publicly available at <https://github.com/BYO-UPM/CUB-Loss>.

CRediT authorship contribution statement

Hua Xu: Writing – original draft, Software, Methodology, Investigation, Formal analysis, Data curation.
 Julián D. Arias-Londoño: Writing – review & editing, Supervision, Methodology, Formal analysis, Conceptualization.
 Juan I. Godino-Llorente: Writing – review & editing, Supervision, Resources, Project administration, Methodology, Funding acquisition, Formal analysis, Conceptualization.

Declaration of competing interest

The authors declare that they have no known competing financial interests or personal relationships that could appear to influence the work reported in this document.

Acknowledgments

This work was supported by the Ministry of Economy and Competitiveness of Spain under grants DPI2017-83405-R1 and PID2021-128469OB-I00, and by Comunidad de Madrid, Spain. Universidad Politécnica de Madrid supports Julián D. Arias-Londoño through a María Zambrano UP2021-035 grant funded by European Union-NextGenerationEU. Hua Xu acknowledges the support provided by the China Scholarship Council. The authors also thank the Madrid ELLIS unit (European Laboratory for Learning & Intelligent Systems) unit for its indirect support. Finally, the authors acknowledge Universidad Politécnica de Madrid for providing computing resources on the Magerit Supercomputer.

References

- [1] Chuan Guo, Geoff Pleiss, Yu Sun, and Kilian Q Weinberger. On calibration of modern neural networks. In *International Conference on Machine Learning (ICML)*, pages 1321–1330, 2017.
- [2] Christian Leibig, Vaneeda Allken, Murat Seçkin Ayhan, Philipp Berens, and Siegfried Wahl. Leveraging uncertainty information from deep neural networks for disease detection. *Scientific Reports*, 7(1):1–14, 2017.

- [3] Marc Combalia, Ferran Hueto, Susu Puig, Josep Malvehy, and Veronica Vilaplana. Uncertainty estimation in deep neural networks for dermoscopic image classification. In *Proceedings of the IEEE/CVF Conference on Computer Vision and Pattern Recognition Workshops*, pages 744–745, 2020.
- [4] David J. C. MacKay. *Bayesian Methods for Adaptive Models*. PhD thesis, California Institute of Technology, Pasadena, CA, 1992.
- [5] Radford M. Neal. *Bayesian Learning for Neural Networks*, volume 118 of *Lecture Notes in Statistics*. Springer, New York, 1996.
- [6] Yarin Gal and Zoubin Ghahramani. Dropout as a Bayesian approximation: Representing model uncertainty in deep learning. In *International Conference on Machine Learning (ICML)*, pages 1050–1059, 2016.
- [7] Charles Blundell, Julien Cornebise, Koray Kavukcuoglu, and Daan Wierstra. Weight uncertainty in neural networks. In *International Conference on Machine Learning (ICML)*, pages 1613–1622, 2015.
- [8] Alex Graves. Practical variational inference for neural networks. In *Advances in Neural Information Processing Systems (NIPS)*, volume 24, pages 2348–2356, 2011.
- [9] Yarin Gal, Jiri Hron, and Alex Kendall. Concrete dropout. In *Advances in Neural Information Processing Systems (NIPS)*, volume 30, pages 3581–3590, 2017.
- [10] Alexander Kurz, Katja Hauser, Hendrik Alexander Mehrtens, Eva Krieghoff-Henning, Achim Hekler, Jakob Nikolas Kather, Stefan Fröhling, Christof Von Kalle, Titus Josef Brinker, et al. Uncertainty estimation in medical image classification: systematic review. *JMIR Medical Informatics*, 10(8):e36427, 2022.
- [11] Ankur Mallick, Chaitanya Dwivedi, Bhavya Kailkhura, Gauri Joshi, and T Yong-Jin Han. Can your ai differentiate cats from covid-19? sample efficient uncertainty estimation for deep learning safety. In *ICML 2020 Workshop on Uncertainty & Robustness in Deep Learning*, 2020.
- [12] Ranganath Krishnan and Omesh Tickoo. Improving model calibration with accuracy versus uncertainty optimization. In *Advances in Neural Information Processing Systems*, volume 33, pages 18237–18248, 2020.
- [13] Xaosong Wang, Yifan Peng, Le Lu, Zhiyong Lu, Mohammadhadi Bagheri, and Ronald Summers. Chestx-ray8: Hospital-scale chest x-ray database and benchmarks on weakly-supervised classification and localization of common thorax diseases. In *2017 IEEE Conference on Computer Vision and Pattern Recognition (CVPR)*, pages 3462–3471, 2017.
- [14] Jeremy Irvin, Pranav Rajpurkar, Michael Ko, Yifan Yu, Silviana Ciurea-Ilcus, Chris Chute, Henrik Marklund, Behzad Haghgoo, Robyn Ball, Katie Shpanskaya, et al. CheXpert: A large chest radiograph dataset with uncertainty labels and expert comparison. In *Proceedings of the AAAI Conference on Artificial Intelligence*, volume 33, pages 590–597, 2019.
- [15] Nour Khalifa, Mohamed Loey, Mohamed Taha, and Hamed Mohamed. Deep transfer learning models for medical diabetic retinopathy detection. *Acta Informatica Medica*, 27(5):327, 2019.
- [16] Philipp Tschandl, Cliff Rosendahl, and Harald Kittler. The HAM10000 dataset, a large collection of multi-source dermatoscopic images of common pigmented skin lesions. *Scientific Data*, 5(1):180161, 2018.
- [17] Taye Girma Debelee. Skin lesion classification and detection using machine learning techniques: A systematic review. *Diagnostics*, 13(19):3147, 2023.
- [18] Aslak Djupskås, Signe Riemer-Sørensen, and Alexander Johannes Stasik. Unreliable Monte Carlo dropout uncertainty estimation. In *Proceedings of the Northern Lights Deep Learning Conference (NLDL)*, Proceedings of Machine Learning Research. PMLR, 2026.
- [19] Diederik P Kingma, Tim Salimans, and Max Welling. Variational dropout and the local reparameterization trick. In *Advances in Neural Information Processing Systems*, volume 28, pages 2575–2583, 2015.
- [20] Max-Heinrich Laves, Sontje Ihler, Karl-Philipp Kortmann, and Tobias Ortmaier. Well-calibrated model uncertainty with temperature scaling for dropout variational inference. In *4th Workshop on Bayesian Deep Learning at NeurIPS*, 2019.
- [21] Max-Heinrich Laves, Sontje Ihler, Karl-Philipp Kortmann, and Tobias Ortmaier. Calibration of model uncertainty for dropout variational inference. *arXiv preprint arXiv:2006.11584*, 2020.
- [22] Tal Zeevi, Ravid Shwartz-Ziv, Yann LeCun, Lawrence H. Staib, and John A. Onofrey. Rate-In: Information-driven adaptive dropout rates for improved inference-time uncertainty estimation. In *Proceedings of the IEEE/CVF Conference on Computer Vision and Pattern Recognition (CVPR)*, pages 20757–20766, 2025.
- [23] Emanuele Ledda, Giorgio Fumera, and Fabio Roli. Dropout injection at test time for post hoc uncertainty quantification in neural networks. *Information Sciences*, 645:119356, 2023.

- [24] Yaniv Ovadia, Emily Fertig, Jie Ren, Zachary Nado, David Sculley, Sebastian Nowozin, Joshua Dillon, Balaji Lakshminarayanan, and Jasper Snoek. Can you trust your model’s uncertainty? Evaluating predictive uncertainty under dataset shift. In *Advances in Neural Information Processing Systems (NeurIPS)*, volume 32, 2019.
- [25] Andrew YK Foong, Yingzhen Li, José Miguel Hernández-Lobato, and Richard E Turner. ‘in-between’ uncertainty in bayesian neural networks. *arXiv preprint arXiv:1906.11537*, 2019.
- [26] Sebastian Farquhar, Michael Osborne, and Yarin Gal. Radial Bayesian neural networks: Beyond discrete support in large-scale Bayesian deep learning. In *Proceedings of the 23rd International Conference on Artificial Intelligence and Statistics (AISTATS)*, volume 108 of *Proceedings of Machine Learning Research*, pages 1352–1362, 2020.
- [27] Florian Wenzel, Kevin Roth, Bastiaan S Veeling, Jakub Swiatkowski, Linh Tran, Stephan Mandt, Jasper Snoek, and Sebastian Nowozin. How good is the bayes posterior in deep neural networks really? In *International Conference on Machine Learning (ICML)*, pages 10248–10259, 2020.
- [28] Archit Karandikar, Nicholas Cain, Dustin Tran, Balaji Lakshminarayanan, Jonathon Shlens, Michael C Mozer, and Becca Weber. Soft calibration objectives for neural networks. In *Advances in Neural Information Processing Systems (NeurIPS)*, volume 34, pages 29768–29779, 2021.
- [29] Max-Heinrich Laves, Sontje Ihler, Karl-Ingo Kortmann, and Tobias Ortmaier. Well-calibrated regression uncertainty in medical imaging with deep learning. In *Medical Imaging with Deep Learning (MIDL)*, pages 393–412, 2020.
- [30] David J. C. MacKay. A practical Bayesian framework for backpropagation networks. *Neural Computation*, 4(3):448–472, 1992.
- [31] Geoffrey E. Hinton and Drew van Camp. Keeping the neural networks simple by minimizing the description length of the weights. In *Proceedings of the 6th Annual Conference on Computational Learning Theory (COLT)*, pages 5–13, 1993.
- [32] Balaji Lakshminarayanan, Alexander Pritzel, and Charles Blundell. Simple and scalable predictive uncertainty estimation using deep ensembles. In *Advances in Neural Information Processing Systems (NeurIPS)*, volume 30, pages 6402–6413, 2017.
- [33] Claude E. Shannon. A mathematical theory of communication. *The Bell System Technical Journal*, 27(3):379–423, 1948.
- [34] Dan Hendrycks and Kevin Gimpel. A baseline for detecting misclassified and out-of-distribution examples in neural networks. In *Proceedings of the International Conference on Learning Representations (ICLR)*, 2017.
- [35] Joanne Cleverley, James Piper, and Melvyn M Jones. The role of chest radiography in confirming covid-19 pneumonia. *BMJ*, 370:m2426, 2020.
- [36] Tulin Ozturk, Muhammed Talo, Eylul Azra Yildirim, Ulas Baran Baloglu, Ozal Yildirim, and U Rajendra Acharya. Automated detection of covid-19 cases using deep neural networks with x-ray images. *Computers in Biology and Medicine*, 121:103792, 2020.
- [37] Camila González, Karol Gotkowski, Moritz Fuchs, Andreas Bucher, Armin Dadras, Ricarda Fischbach, Isabel Jasmin Kaltenborn, and Anirban Mukhopadhyay. Distance-based detection of out-of-distribution silent failures for covid-19 lung lesion segmentation. *Medical Image Analysis*, 82:102596, 2022.
- [38] Alistair EW Johnson, Tom J Pollard, et al. MIMIC-CXR, a de-identified publicly available database of chest radiographs with free-text reports. *Scientific Data*, 6:317, 2019.
- [39] Linda Wang, Zhong Qiu Lin, and Alexander Wong. Covid-net: a tailored deep convolutional neural network design for detection of covid-19 cases from chest x-ray images. *Scientific Reports*, 10(1):19549, 2020.
- [40] Joseph Paul Cohen, Paul Morrison, Lan Dao, Karsten Roth, Tim Q Duong, and Marzyeh Ghassemi. Covid-19 chest x-ray dataset initiative. <https://github.com/ieee8023/covid-chestxray-dataset>, 2020. Dataset.
- [41] Agam Chung et al. Actualmed covid-19 chest x-ray dataset initiative. <https://github.com/agchung/Actualmed-COVID-chestxray-dataset>, 2020. Dataset.
- [42] Muhammad E. H. Chowdhury, Tawsif R. Rahman, Amith Khandakar, Rashid Mazhar, et al. Covid-19 radiography database – version 3. <https://www.kaggle.com/datasets/tawsifurrahman/covid19-radiography-database>, 2020. Dataset.
- [43] RSNA and Society of Thoracic Radiology. Rsna pneumonia detection challenge dataset. <https://www.kaggle.com/c/rsna-pneumonia-detection-challenge>, 2018. Dataset.

[44] María de la Iglesia Vayá, José M. Saborit, Joaquim Á. Montell, Antonio Pertusa, Aurelia Bustos, Miguel Cazorla, Joaquin Galant, Xavier Barber, Domingo Orozco-Beltrán, Francisco García-García, Marisa Caparrós, Germán González, and Jose M. Salinas. Bimcv-covid19+: A large annotated dataset of rx and ct images of covid-19 patients. <http://bimcv.cipf.es/bimcv-projects/bimcv-covid19>, 2020. Dataset.

[45] Jacob Saltz, Michael Saltz, Pranav Prasanna, Richard Moffitt, John Hajagos, et al. Stony brook university covid-19 positive cases (covid-19-ny-sbu). <https://doi.org/10.7937/TCIA.BBAG-2923>, 2021. Dataset.

[46] Julián D Arias-Londoño and Juan I Godino-Llorente. Analysis of the clever hans effect in covid-19 detection using chest x-ray images and bayesian deep learning. *Biomedical Signal Processing and Control*, 90:105831, 2024.

[47] Jingyang Zhang, Jingkang Yang, Pengyun Wang, Haoqi Wang, Yueqian Lin, Haoran Zhang, Yiyou Sun, Xuefeng Du, Yixuan Li, Ziwei Liu, Yiran Chen, and Hai Li. OpenOOD v1.5: Enhanced benchmark for out-of-distribution detection. *Journal of Data-centric Machine Learning Research*, 2, 2024.

[48] Terrance DeVries and Graham W. Taylor. Learning confidence for out-of-distribution detection in neural networks. *arXiv preprint arXiv:1802.04865*, 2018.

[49] David Macêdo, Tsang Ing Ren, Cleber Zanchettin, Adriano L. I. Oliveira, and Teresa Ludermir. Entropic out-of-distribution detection: Seamless detection of unknown examples. *IEEE Transactions on Neural Networks and Learning Systems (TNNLS)*, 33(6):2350–2364, 2022.

[50] Harry Anthony and Konstantinos Kamnitsas. On the Use of Mahalanobis Distance for Out-of-distribution Detection with Neural Networks for Medical Imaging. In Carole H. Sudre, Christian F. Baumgartner, Adrian Dalca, Raghav Mehta, Chen Qin, and William M. Wells, editors, *Uncertainty for Safe Utilization of Machine Learning in Medical Imaging*, pages 136–146. Springer Nature Switzerland, 2023.

[51] Shiyu Liang, Yixuan Li, and R. Srikanth. Enhancing the reliability of out-of-distribution image detection in neural networks. In *International Conference on Learning Representations (ICLR)*, 2018.

[52] Kun Fang, Qinghua Tao, Kexin Lv, Mingzhen He, Xiaolin Huang, and Jie Yang. Kernel PCA for out-of-distribution detection. In *Advances in Neural Information Processing Systems (NeurIPS)*, 2024.

[53] Mohsin Akram, Muhammad Adnan, Syed Farooq Ali, Jameel Ahmad, Amr Yousef, Tagrid Abdullah N. Alshalali, and Zaffar Ahmed Shaikh. Uncertainty-aware diabetic retinopathy detection using deep learning enhanced by bayesian approaches. *Scientific Reports*, 15(1):1342, 2025.

[54] Asia Pacific Tele-Ophthalmology Society. APTOS 2019 blindness detection. <https://www.kaggle.com/c/aptos2019-blindness-detection>, 2019.

[55] Sovit Rath. Diabetic retinopathy 224x224 gaussian filtered. <https://www.kaggle.com/datasets/sovitrath/diabetic-retinopathy-224x224-gaussian-filtered>, 2019.

[56] Yarin Gal. *Uncertainty in deep learning*. PhD thesis, University of Cambridge, 2016.

[57] Usharani Bhimavarapu, Nalini Chintalapudi, and Gopi Battineni. Automatic detection and classification of diabetic retinopathy using the improved pooling function in the convolution neural network. *Diagnostics*, 13(15):2606, 2023.

[58] G. Alwakid, W. Gouda, M. Humayun, and N.Z. Jhanjhi. Enhancing diabetic retinopathy classification using deep learning. *Digital Health*, 9:20552076231203676, 2023.

[59] José Escorcia-Gutierrez, Jose Cuello, Carlos Barraza, Margarita Gamarra, Pere Romero-Aroca, Eduardo Caicedo, Aida Valls, and Domènec Puig. Analysis of pre-trained convolutional neural network models in diabetic retinopathy detection through retinal fundus images. In Khalid Saeed and Jiří Dvorský, editors, *Computer Information Systems and Industrial Management*, pages 202–213. Springer International Publishing, 2022.

[60] K Ruwani M Fernando and Chris P Tsokos. Dynamically weighted balanced loss: Class imbalanced learning and confidence calibration of deep neural networks. *Diagnostics*, 11(8):1242, 2021.

[61] Ranganath Krishnan, Mahesh Subedar, and Omesh Tickoo. Specifying Weight Priors in Bayesian Deep Neural Networks with Empirical Bayes. In *Proceedings of the AAAI Conference on Artificial Intelligence*, volume 34, pages 4477–4484, 2020.

[62] Ravid Shwartz-Ziv, Micah Goldblum, Hossein Souri, Sanyam Kapoor, Chen Zhu, Yann LeCun, and Andrew G Wilson. Pre-train your loss: Easy bayesian transfer learning with informative priors. *Advances in Neural Information Processing Systems*, 35:27706–27715, 2022.